

Article

Heat Transfer Optimization of NEXA Ballard Low-Temperature PEMFC

Artem Chesalkin ^{1,*}, Petr Kacor ² and Petr Moldrik ²

¹ ENET Centre—Research Centre of Energy Units for Utilization of Non Traditional Energy Sources, VŠB-TUO, 17. Listopadu 2172/15, 708 00 Ostrava-Poruba, Czech Republic

² Department of Electrical Power Engineering, VŠB-TUO, 17. Listopadu 2172/15, 708 00 Ostrava-Poruba, Czech Republic; petr.kacor@vsb.cz (P.K.); petr.moldrik@vsb.cz (P.M.)

* Correspondence: artem.chesalkin@vsb.cz

Abstract: Hydrogen is one of the modern energy carriers, but its storage and practical use of the newest hydrogen technologies in real operation conditions still is a task of future investigations. This work describes the experimental hydrogen hybrid energy system (HHS). HHS is part of a laboratory off-grid system that stores electricity gained from photovoltaic panels (PVs). This system includes hydrogen production and storage units and NEXA Ballard low-temperature proton-exchange membrane fuel cell (PEMFC). Fuel cell (FC) loses a significant part of heat during converting chemical energy into electricity. The main purpose of the study was to explore the heat distribution phenomena across the FC NEXA Ballard stack during load with the next heat transfer optimization. The operation of the FC with insufficient cooling can lead to its overheating or even cell destruction. The cause of this undesirable state is studied with the help of infrared thermography and computational fluid dynamics (CFD) modeling with heat transfer simulation across the stack. The distribution of heat in the stack under various loads was studied, and local points of overheating were determined. Based on the obtained data of the cooling air streamlines and velocity profiles, few ways of the heat distribution optimization along the stack were proposed. This optimization was achieved by changing the original shape of the FC cooling duct. The stable condition of the FC stack at constant load was determined.

Keywords: hydrogen; fuel cells; hydrogen hybrid energy system; thermography; CFD modeling; heat transfer; optimization



Citation: Chesalkin, A.; Kacor, P.; Moldrik, P. Heat Transfer Optimization of NEXA Ballard Low-Temperature PEMFC. *Energies* **2021**, *14*, 2182. <https://doi.org/10.3390/en14082182>

Academic Editors: Samuel Simon Araya and Jinliang Yuan

Received: 11 February 2021

Accepted: 12 April 2021

Published: 14 April 2021

Publisher's Note: MDPI stays neutral with regard to jurisdictional claims in published maps and institutional affiliations.



Copyright: © 2021 by the authors. Licensee MDPI, Basel, Switzerland. This article is an open access article distributed under the terms and conditions of the Creative Commons Attribution (CC BY) license (<https://creativecommons.org/licenses/by/4.0/>).

1. Introduction

Hydrogen technologies find their use in a wide range of mobile and stationary applications. One of the most developing and applied ways for renewable energy storage is a way of electrochemical energy storage [1]. Hydrogen hybrid systems (HHSs) can utilize renewable energy sources (RESs) and eliminate the fluctuations of their power output by energy storage in form of hydrogen. These types of hybrid systems were examined and tested by the authors in different studies [2–4]. Typically, HHSs consist of energy production units from RESs, combined with hydrogen production and storage unit for power-to-gas conversion (PtG), fuel cell (FC) unit, and classical backup energy storage in a battery bank [5].

The proton-exchange membrane fuel cell (PEMFC) is a promising, widely developed type of the FC that could be operated at the relatively wide temperature range and uses “green” hydrogen as an alternative energy carrier for the grid-connected and off-grid installations [6]. Cells are often combined in series—FC stack [7–9]. Figure 1 shows a simplified diagram of the hydrogen PEMFC in terms of its design and principle of operation, where FP—flow plates, GDL—gas diffusion layers, and CL—catalyst layers.

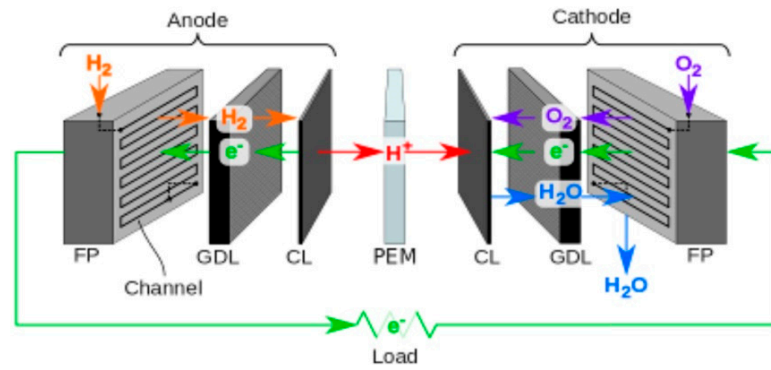


Figure 1. Construction and principle of hydrogen proton-exchange membrane fuel cell (PEMFC) [10,11].

Fuel cells use direct conversion of chemical energy into electric power, and that is the reason for their high efficiency and almost no emissions. The main type of FC emission is a thermal emission that occurs during FCs operation, especially at high loads. The FC voltage as a function of current density can be seen in Figure 2 below, where OCV is the open-circuit voltage. The value of 1.2 V represents a theoretically loss-free voltage. The actual cell voltage, including the off-load voltage, is always lower than this value.

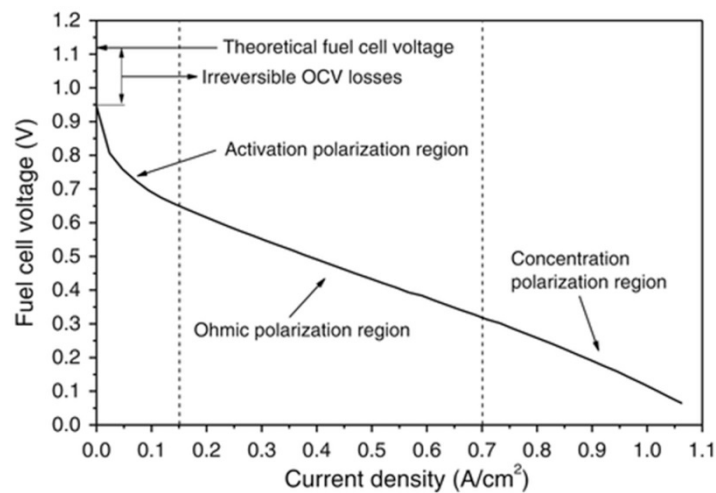


Figure 2. Fuel Cell (FC) polarization curve with voltage losses during FC load [12].

Each FC can produce the maximum theoretical voltage of 1.187 V (for 25 °C and 101.325 kPa). The FC efficiency is calculated as the ratio of the actually produced and the theoretically achievable cell voltage

$$\eta = \frac{V_{real}}{E_{cell}} = \frac{V_{real}}{1.187} \quad (1)$$

where E_{cell} refers to the voltage in every cell related to the Gibbs free energy. The real voltage in an actual cell is measured at the power load per cell as $V_{real} = 0.5\text{--}0.6$ V. The off-load voltage reaches the value of 1.1 V [13]. The typical service electrochemical efficiency per cell is approximately between 40% and 50% [14].

Studied NEXA Ballard PEMFC uses the air-based heat exchange system for stack cooling. High-temperature PEMFC provides easier heat regulation, in comparison with studied low-temperature PEMFC, due to higher working temperatures and using liquid refrigerants for stack cooling [15–17].

Several studies were focused on hydrogen storage methods development. In some cases, due to space limitation and pressure-based safety restrictions, it is possible to use hydrogen storage in a solid-state way in metal hydrides (MHs) [18–20]. Joint use of fuel cell

(FC) technologies with hydrogen storage systems based on metal hydrides (MHs) allows the utilization of FC excess heat energy for the MH hydrogen desorption process and thereby increases the HHS energy efficiency. MHs application for solar energy accumulation is one of the possible ways described by the authors in various papers [21,22]. In addition, using FCs and MHs in one system gives the possibility to provide the required pure hydrogen to the PEMFCs. LaNi—based alloys allow storing hydrogen at ambient temperatures of 25–40 °C and low pressures of 1.0–1.5 MPa, which makes the application of these alloys quite attractive in mentioned above specific conditions [23–28].

The complete experimental setup described in the work is an integral hydrogen hybrid system, which serves for the possibility of optimal energy storage from solar panels in various forms—in the form of electrical energy for direct use or storage in storage batteries, or in the form of gaseous hydrogen in classical gas cylinders and/or in a compact “solid” form in the form of metal hydrides.

One of the main components of this system is fuel cells and the associated fuel source, hydrogen, which, as mentioned above, can be stored in various forms. During the operation of the hybrid plant, overheating of the fuel cells was detected at loads close to maximum and automatic shutdown of fuel cells was observed at high loads when the ambient temperature rose above 25 degrees, while the maximum operating ambient temperature for this fuel cell declared in the documentation was 30 degrees. In this regard, the analysis of the fuel cell and the identification of local overheating zones were started, followed by the simulation of heat transfer along the entire stack of the fuel cell and modification of the elements of the cooling channel.

The main motivation of the work is the improvement in the FC cooling and heat transfer along the FC stack, which is an important issue of safe and efficient operation of the FC and hydrogen hybrid system (HHS) [29–31]. Experimental HHS was developed for joint MH and FC testing. This system, shown in Figure 3, basically consists of photovoltaic panels (PVs), a few power inverters batteries bank, hydrogen production, and storage units. Hydrogen could be stored in three different ways—in pressure vessels in a gaseous state, in metal hydrides in solid state, or converted to electricity via FC and directly used or stored in the battery bank. The lead batteries accumulation enables the storage of 550 kWh of power, and an additional 80 kWh can be stored in the lithium iron phosphate (LiFePO) batteries bank, which provides energy accumulation from the PV plant and avoid energy fluctuation for the stable H₂ production via water electrolysis process.

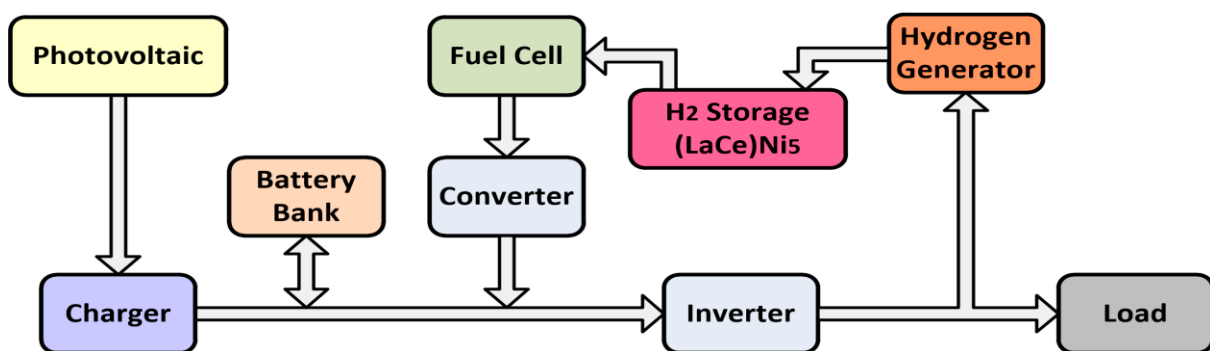


Figure 3. The basic scheme of the experimental hybrid energy system (HHS) energetic system.

According to the nameplate, the ambient operating temperature of the cell must be in the range of 3–30 °C. At a temperature around 22–25 °C, the maximum operating state cannot be reached due to local overheating of the PEMFC in its front part. This was the main reason to make an FC heat transfer optimization for more uniform stack cooling. The FC heat transfer could be studied using infrared (IR) thermography and appropriate PEMFC computational fluid dynamics (CFD) modeling [32]. IR thermography has been widely used in different industrial and research fields including analysis and cracks determine

in membrane materials and characterizing of PEMFC parameters [33–36]. Increasing the efficiency of FC cooling is indeed a popular topic in scientific studies and can be found in a number of literature sources [37,38]. Unfortunately, many authors focus their studies on the single cell and rarely assess the behavior of the PEMFC stack as a whole; therefore, the study of more uniform stack cooling was the main goal on the way of the FC heat transfer optimization.

2. Testing and Measurement Methods

The thermal field distribution over the low-temperature PEMFC was measured by the FLIR E45 thermal camera. The hydrogen produced via the anion-exchange membrane (AEM) electrolyzer with an output pressure of 3.0 MPa before entering the MH storage system or PEMFC passes through the pressure reducer. Heat field distribution across the surface of the PEMFC body was controlled by IR thermo-vision camera. Laboratory measurements of the heating curves of the NEXA module were conducted according to the block diagram shown in Figure 4.

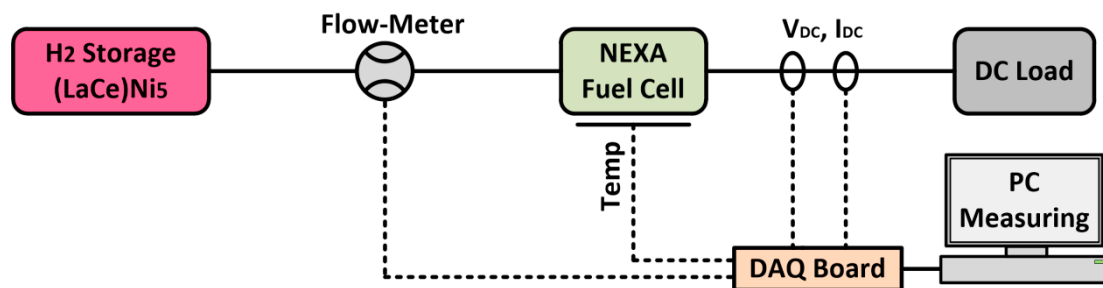


Figure 4. Diagram of the PEMFC heating distribution measurement.

The following measurements were conducted on the NEXA power module of PEMFC: Rated DC power output of this system is 1200 W; operating voltage range of the system is from 26 V (at rated power) to 42 V (no-load voltage); the total numbers of 47 cells are connected in series into the stack. The system further comprises ancillary equipment necessary for its operation, i.e., control unit, hydrogen delivery system, oxidant air supply, and cooling air supply (by cooling fan and compressor). The working parameters of the studied NEXA Ballard PEMFC are shown in Table 1.

Table 1. The main working parameters of fuel cells and hydrogen storage system [39].

NEXA Ballard LT PEMFC	
Characteristic	Value
Operation Temperature	65 °C
Rated Power	1200 W
Maximum Current I	230 A
Operating Voltage U	22–50 V
Active Area	120 cm ²
Max. H ₂ Consumption	18.5 L min ⁻¹
H ₂ Pressure	70–120 kPa

3. Experimental and Simulation Results

The measuring procedure consisted of measurements of the load characteristics of the NEXA module, its hydrogen and oxidant air consumption, water production, and the self-power consumption, which shows the relation of the power output drawn by the NEXA module from its own stack to ensure the operation of its own auxiliary devices at the certain power output. Figure 5 shows the load characteristics of the NEXA module. This module has soft source properties; the voltage of 42 V (at no load) drops to 26 V (at a rated power of 1200 W).

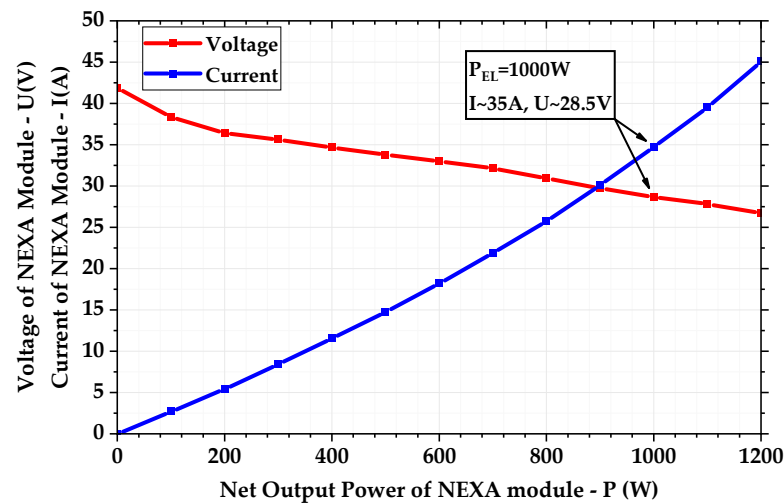


Figure 5. Load characteristics of NEXA FC stack.

The fuel consumption shown in Figure 6 has been determined from the mass flow meter with an integration member after the so-called cells purging. FC was purged with H_2 once the voltage has dropped below a certain level to restore the higher voltage in cells again. The above-mentioned purge deprives cells of impurities and water on a regular basis since those are accumulated on electrode surfaces to intercept the electrochemical reaction. The frequency of purges rises with the increase of FC power output. The fuel used for this cleaning is drained out of the system. This amount of H_2 is included in the overall fuel consumption. The maximum H_2 consumption rate of the NEXA module is 18.5 L min^{-1} . This consumption rate is proportional to the net output power of the NEXA module. The maximum air consumption rate is 90 L min^{-1} at rated power. The FC consumes O_2 from the ambient air.

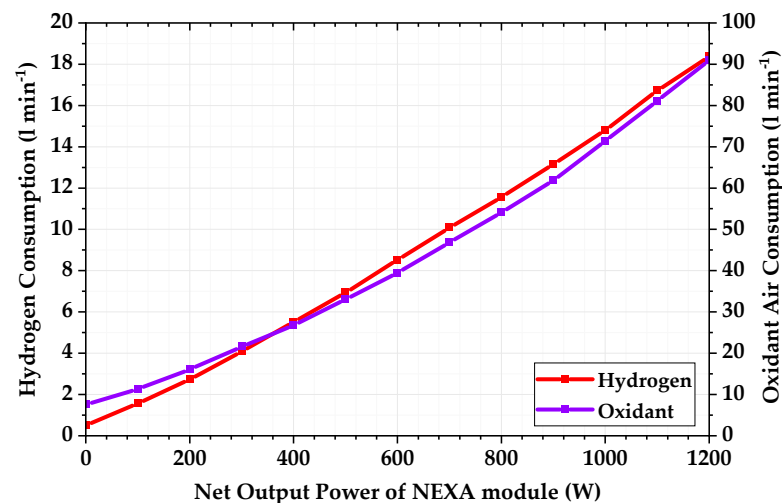


Figure 6. Fuel (hydrogen) and oxidant air consumption of NEXA FC stack.

NEXA FC stack provides power for its own support system, which consists of an oxidant air pump, cooling fan, sensors, and controllers. The required auxiliary power is 39 W (at no load). This self-power consumption increases with increasing load and is shown in Figure 7. The required auxiliary power is 290 W at rated power. The main electrical appliances include an air pump and cooling fan. The gross power of the NEXA module is given by the sum of the net output power at the module terminals and the power consumption of the module itself.

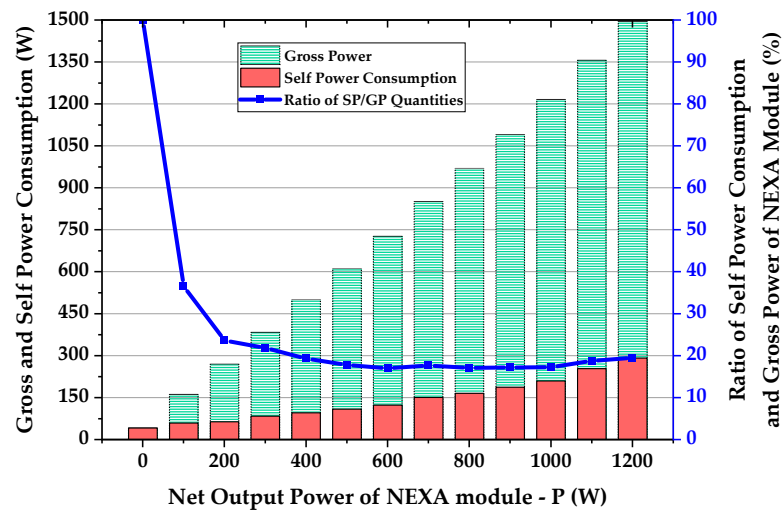


Figure 7. Gross power and self-consumption of NEXA FC stack.

In addition, the NEXA power module efficiency is presented in Figure 8. This efficiency is defined by the ratio of the net output power of the NEXA module to the lower heating value (LHV) of H_2 consumed in the reaction. In the production of electricity from H_2 , the NEXA module achieves the maximum efficiency at partial load (approx. 300 W). The efficiency decreases at higher—but also lower—loads than the stated 300 W. In the second case, in which the decrease is more dramatic, this is due to a larger ratio of the NEXA module's self-consumption to the amount of H_2 consumed. At maximum load (i.e., at rated power of 1200 W), the NEXA module has an efficiency of approx. 38%.

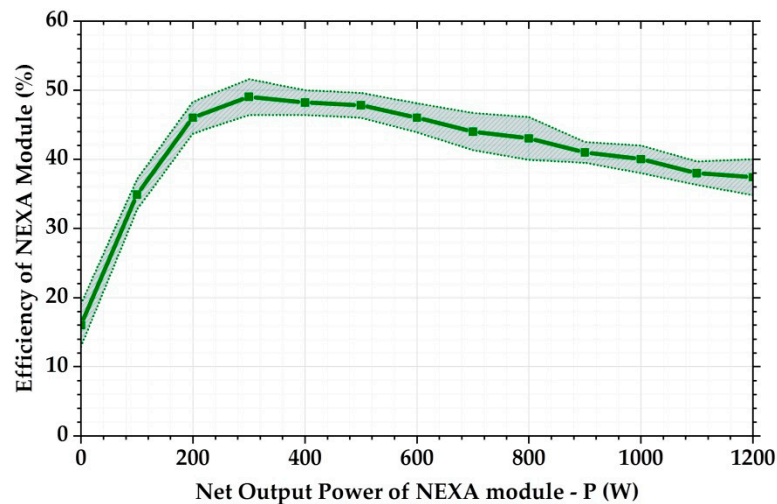


Figure 8. The output efficiency of the NEXA FC stack.

NEXA low-temperature (LT) PEMFC thermography measurements were taken at different loads set on the linked electronic DC load of 100 W, 300 W, 500 W, and 1000 W. FC temperature was measured at the cathode air exhaust of the stack.

There is no local overheating at low or middle PEMFC loads (in the range of 100–500 W), and the presented cooling system seems to be sufficient. The obtained IR thermograms show significant temperature differences between parts of the stack at higher loads; see Figure 9. The left side of the stack, located closer to the entry of the cooling air supply channel, heats up significantly more. At maximum PEMFC loads (in range of 1000–1200 W), the operation temperature of the FC reaches its limit, and FC work stops due to the thermal protection of the system. On the front side of the cooling fins, shown in Figure 9b, local

overheating is visible (marked as a rectangle). The maximum value of temperature is approximately $T = 338$ K.

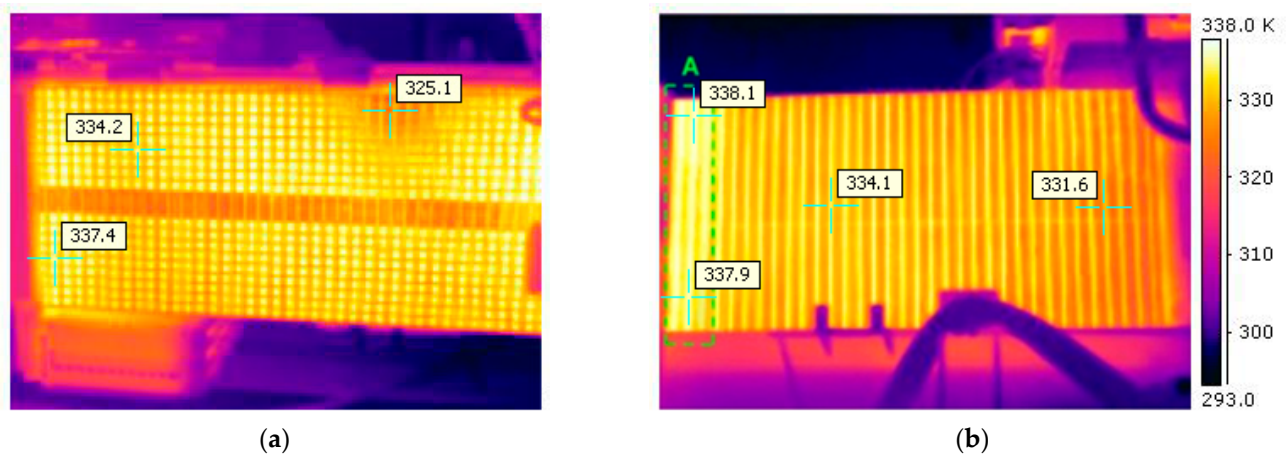


Figure 9. NEXA PEMFC stack infrared (IR)-thermography at $P = 1000$ W: (a) top view and (b) side view.

FC CFD Heat Transfer Simulation and Cooling Duct Optimization

Unequal heating of the FC stack module, detected by IR-thermography measurement, was studied by computed fluid dynamics (CFD) modeling and analyzed using the ANSYS software. The simulation determined the temperature distribution within the NEXA Ballard LT PEMFC stack. The cooling airflow velocity inside the cooling channel and cooling fins was studied. The simulation was performed at the higher problematic $P_{el} = 1000$ W load. The 47 cells connected in series form a system of channels for cooling air circulation and heat dissipation from the stack. The cooling duct for airflow circulation made from a plastic shell is located below the FC module. This plastic frame acts as well as an FC module mounting system. The inlet of the cooling channel has a shape of a rectangle hole with a dimension of $W \times H = 120 \times 80$ mm. A radial fan is mounted near the inlet of the cooling duct. All walls of the cooling duct are smooth and only the bottom side has a glued roughness surface.

Two small plastic attachments are molded on the inlet of the cooling duct and shown in Figure 10. These attachments make high distortion of the cooling streamlines, which lead to a decrease in the cooling efficiency of the system. The low cooling efficiency at the front side of the FC stack increases the temperature of cooling fins. This phenomenon was previously detected by the infrared (IR) measurements and shown in Figure 9b.

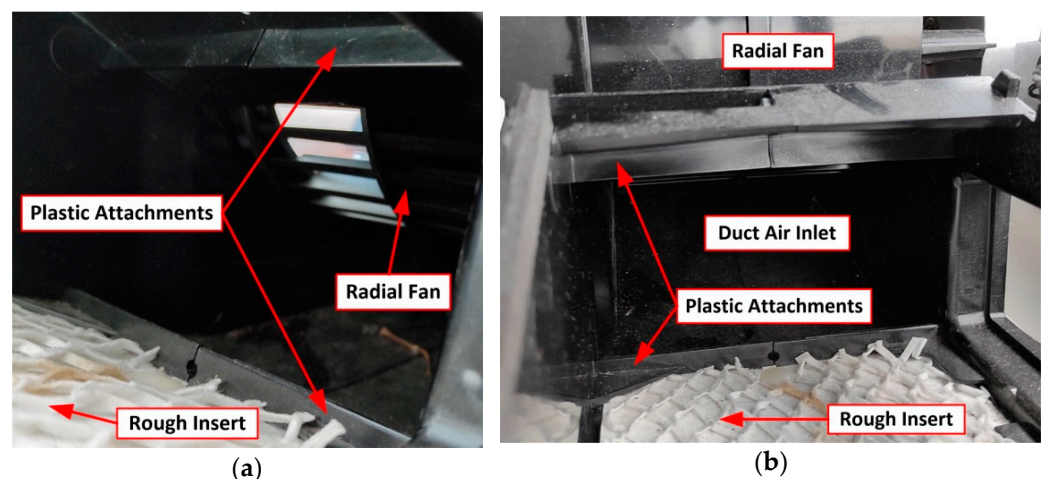


Figure 10. Interior of the cooling duct close to the fan outlet. (a) side view and (b) front view.

It is obvious that the presented cooling system needs to be improved to minimize the stack overheating during operation and at higher loads. One way to improve the FC cooling and heat transfer along the stack is to optimize the shape of the cooling duct. Another condition that should be met is using the original design of a radial fan without its replacement.

The model of the FC stack was designed via SolidWorks software. To simulate the performance of the NEXA PEMFC cooling system, fluid dynamics and thermal analysis were performed using the numerical model on the ANSYS CFX software. This model solves discrete Reynolds averaged Navier–Stokes equations to simulate the flow of the air coolant (heat transfer) along the stack. The governing equations are solved with a standard $k-\epsilon$ model for turbulence modeling. Simultaneously, the energy equation is also solved to determine the heat transfer in both solid and fluid regions [40,41]. The basic 3D model of the cooling duct including PEM and cooling fins is depicted in several view sections in Figure 11.

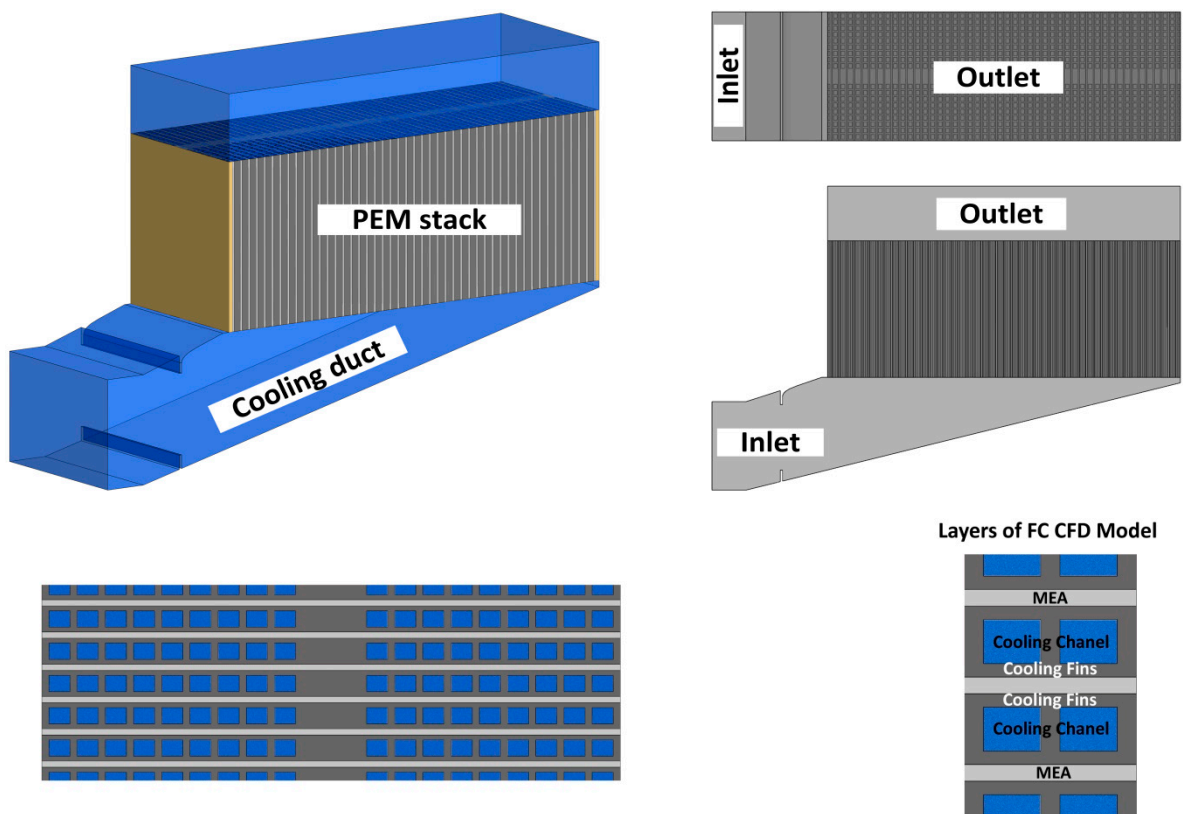


Figure 11. Geometric model of NEXA PEMFC stack used for computational fluid (CFD) simulation and optimization.

Internal power losses caused by chemical reactions in PEMFC and Joule's losses produced by electric current inside the cooling fins were modeled by heat sources in mentioned solid components. Internal heat generation is set according to the selected load $P_{el} = 1000$ W. The PEMFC current and output voltage at that load point can be found in Figure 5 ($P_{el} = 1000$ W; $V_1 = 28.5$ V; $I_1 = 35$ A; $V_{CELL} = 0.606$ V). The generated heat is calculated by the following equation [42,43]:

$$Q_{GEN} = (1.254 - V_{CELL})I_1 = P_{EL} \left(\frac{1.254}{V_{CELL}} - 1 \right) \quad (2)$$

$$Q_{GEN} = 1000 \left(\frac{1.254}{0.606} - 1 \right) = 1063 \text{ W} \quad (3)$$

All considered values of power losses and material properties that have been used for modeling are listed in Table 2.

Table 2. Material properties and power loss values used for CFD modeling [11,16].

FC Construction Parts	External Plates (Golden Coated)	Cooling Fins (Graphite/Composite)	MEA (Polymer)
Thermal Conductivity, [W (m K) ⁻¹]	318	95	0.185
Power Losses, [W]	-	410	650
Volume of the Component, [m ³]	-	1.08 × 10 ⁻³	0.43 × 10 ⁻³
Unit Loss, [W m ⁻³]	-	0.37 × 10 ⁶	1.50 × 10 ⁺⁶

The fluid domain was modeled with air as a coolant at atmospheric conditions. Part of the heat is dissipated via external areas (walls) of PEMFC by natural convection. This fact is taken into account and included in the heat transfer coefficient applied to all vertical walls of the PEMFC CFD model. For vertically oriented surfaces with natural convection conditions, the heat transfer coefficient depends on the Nusselt number, that is, properties of the coolant, geometry of the passages, and flow characteristics. The temperature dependence of the heat transfer coefficient can be evaluated by a combination of the Nusselt, Prandtl, and Rayleigh numbers [36] as follows:

$$h = \frac{k}{L} \cdot Nu_L \quad (4)$$

$$Ra_L = \frac{g\beta(T_S - T_0)L^3}{\nu\alpha} \quad (5)$$

$$Pr = \frac{\nu}{\alpha} \quad (6)$$

$$Nu_L = \left\{ 0.825 + \frac{0.387Ra_L^{1/6}}{\left[1 + \left(\frac{0.5}{Pr}\right)^{9/16} \right]^{8/27}} \right\}^2 \quad (7)$$

where h —heat transfer coefficient (W m⁻² K⁻¹); g —gravity (m s⁻²); β —thermal expansion coefficient (K⁻¹); L —characteristic length (m); ν —kinematic viscosity (m² s⁻¹), α —thermal diffusivity (m² s⁻¹); T_S —surface temperature (K); and T_0 —surroundings temperature (K). Figure 12a shows the application of heat transfer coefficient on external areas of the proton-exchange membrane (PEM) and Figure 12b shows its temperature dependence derived from Equations (4)–(7).

The CFD analysis requires high-density mesh, especially inside of all fluid parts. The velocity gradient reaches high values in the solid–fluid layers, and any coarse mesh may cause serious inaccuracy of the calculation and complicate the convergence. In this regard, the inflations of mesh cells at each transition between fluid–solid parts were applied.

Figure 13a shows the distribution of air velocity at the cross section of the front part of the original FC stack cooling duct. The mentioned figure shows a phenomenon of the swirling streamlines behind the plastic attachments. The airflow is interrupted in the front part of the cooling fins. The situation is similar in the top and bottom sides of the cooling duct. A number of the performed simulations showed the reverse airflow from cooling fins because of the low pressure behind the plastic attachments. Both CFD in Figure 13b and IR in Figure 9b temperature analysis of the NEXA PEMFC stack show the local overheating at the front part of cooling fins due to the intensive swirling of the airflow.

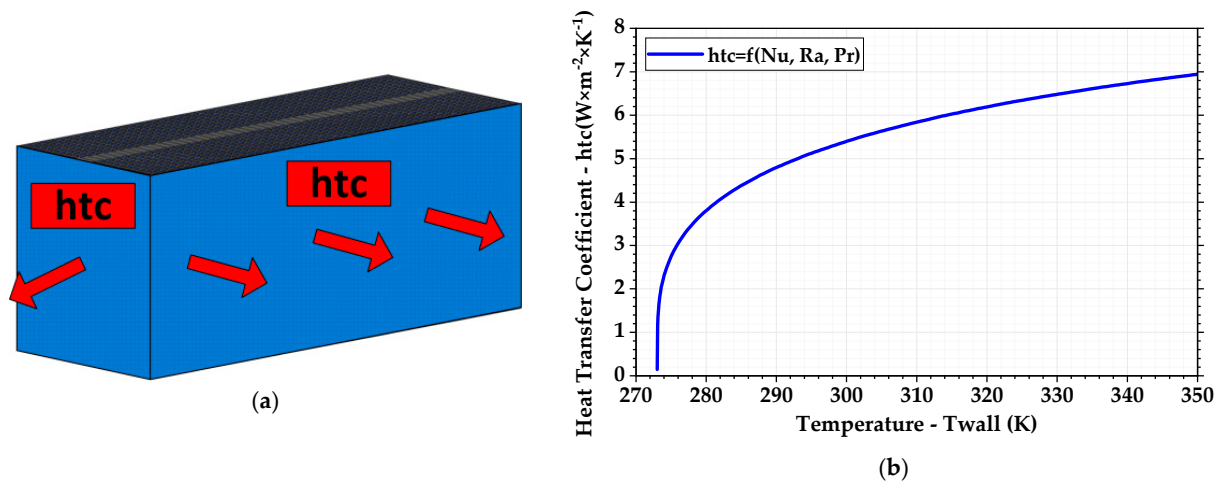


Figure 12. Applying heat transfer coefficient for external surfaces of the stack (a) application on external areas, (b) temperature dependence of heat transfer coefficient.

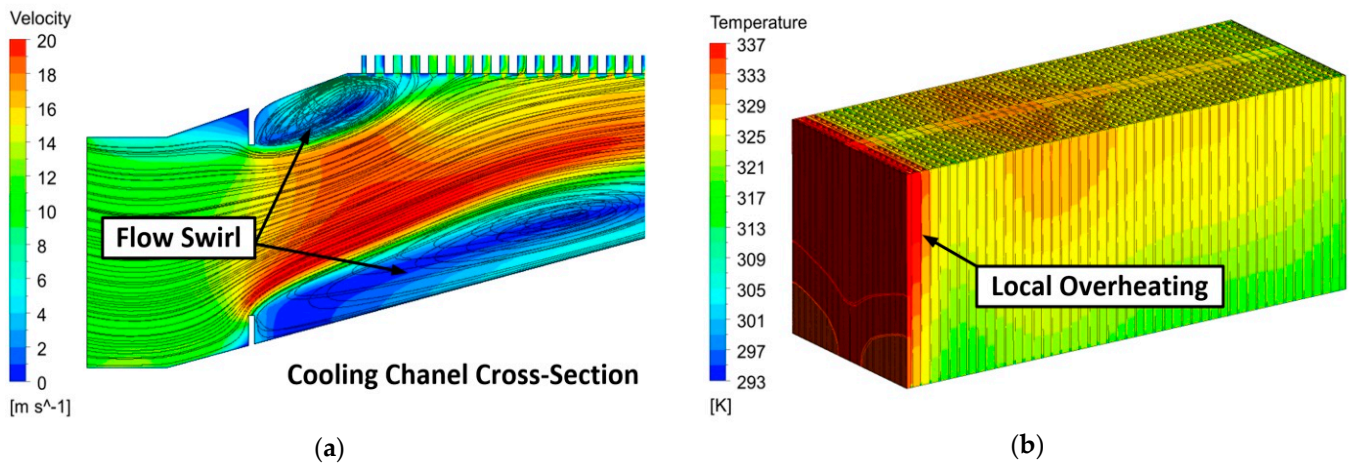


Figure 13. (a) Streamlines of the air coolant and (b) temperature distribution at $P_{el} = 1000$ W of load.

In the simulated model, the temperature differences are somewhat slightly higher. This is mainly due to the applied simplification of the CFD model, which does not take into account the complex construction of a real PEMFC. Additional devices (humidifier, control card, sensors, etc.) are placed on the sidewalls of the PEMFC structure, which generally decrease the heat dissipation to the surroundings and thus increase its overall temperature.

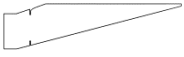





In the CFD model, temperature-dependent heat transfer coefficients have been applied to the entire walls of the PEMFC stack, and the CFD model is generally better cooled. Thus, the simulated temperature distribution and values on our model differ. In the CFD model, we emphasized a precise computing network (mesh) in the air duct and the boundary layer between fluid and solid objects. The model contains more than 15 million elements, and its solution is very time consuming. We believe that even with this simplification in the construction of the model, there can be found a fairly good match with real PEMFC.

The internal plastic attachments are the integrated part of the radial fan assembly and cannot be simply removed. It is possible to slightly modify its height. To increase the airflow rate to the front part of the stack, the shape modification of the airflow streamlines has to be made. The airflow adjustment can be realized without any significant disruption of the original duct design by using appropriately formed inserts (wings) and blades placed into the cooling duct.

Several modifications of the adjustments in the inlet part of the cooling duct and in its interior have been simulated. The basis of all analyzed modifications was the insertion

of variously shaped blades, which direct the flow of cooling air. Each of the mentioned options was also dimensionally modified (length of the blades, their inclination angle, and position in the cooling channel, etc.). Table 3 shows the list of the analyzed modification of the FC cooling duct.

Table 3. Analyzed modification of the cooling duct of PEMFC.

Cooling Duct Modification						
Applied Change	Original	Skewed Airfoil	Skewed Airfoil and Blades	Round and Straight Blades	Round Cover and Straight Blades	Round Cover and 3 Short Blades
Decreasing of Temperature	-	0	1	1	1	1
Simple Design Overall	-	1	0	0	1	1
Improvement	-	0	1	1	0	1
Final Decision	-	No	No	Yes	No	Yes
Type of Modification	-			A		B

The two most appropriate solutions of the cooling duct adjustment (Type A and Type B) are depicted in Figure 14.

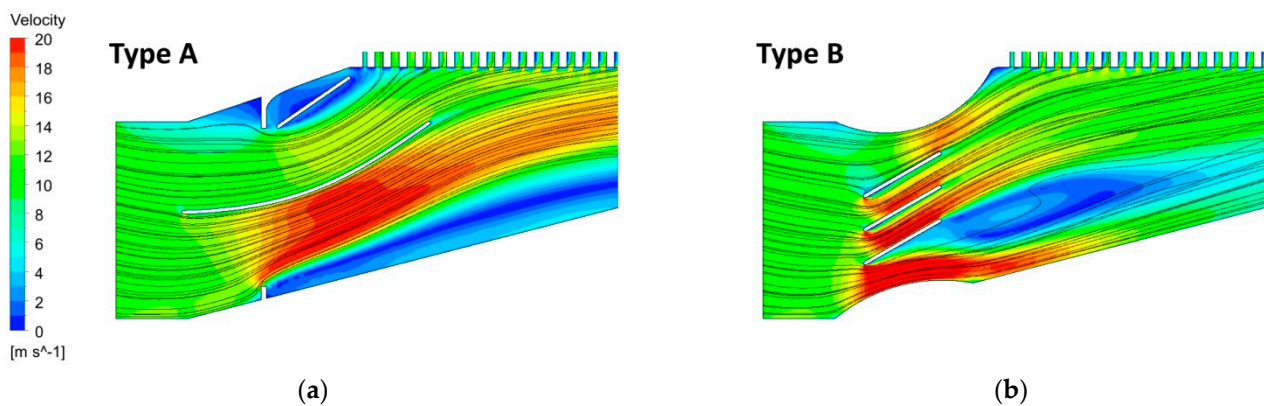


Figure 14. Streamlines and velocity profile of the modified cooling duct in (a) Type A and (b) Type B.

Figure 14 shows streamlines and velocity profiles at the input side of the cooling duct cross section. Type A modification, shown in Figure 14a, contains two additional blades. One of the blades is slightly curved and located in the center of the cooling duct. The second one has a straight shape and creates the covering of the top plastic attachment. The bottom plastic attachment is also lowered by cutting. The used system of blades in Type A modification serves especially for suitable airflow direction to the front part of the PEM stack cooling fins. Type B modification, shown in Figure 14b, is created by covering the top and bottom plastic attachment with a round surface. The rounded surface is simply made from the appropriate cut thin PVC tube. These tube pieces are glued to the internal surface of the cooling duct and easily create an effective shape for airflow. To intensify the direction of the streamline, three additional blades in the center of the cooling duct were used. The swirl occurs behind of bottom blade, but it also gradually disappears with increasing the length of the channel.

Figure 15 shows how cooling duct modification changes the temperature distribution. The local overheating at the front side of PEM, shown in Figure 15b, that corresponded to the original design of the cooling duct has been removed. The area with a higher temperature is now closer to the middle of the PEM assembly. The maximal value of temperature is also decreased in the range of 7 K, from $T_1 = 338$ K in the original design to

$T_2 = 331$ K in Type A and Type B modifications. Type B modification also shows the better temperature distribution along the stack, without any significant local temperature rise. Moreover, the round surfaces and straight blades in Type B modification can be simply manufactured in comparison to the complicated shaping of a curved blade used in Type A.

Figure 16 shows the temperature distribution and velocity profile on the section area located near the coolant outlet (approx. $H = 5$ mm). Both Type A and Type B duct modifications improve the airflow in the front part of PEMFC, which is visible mainly on the velocity profile. The temperature here also reaches lower values in comparison to the rest part of the section area. Important values of performed simulations are collected in Table 4.

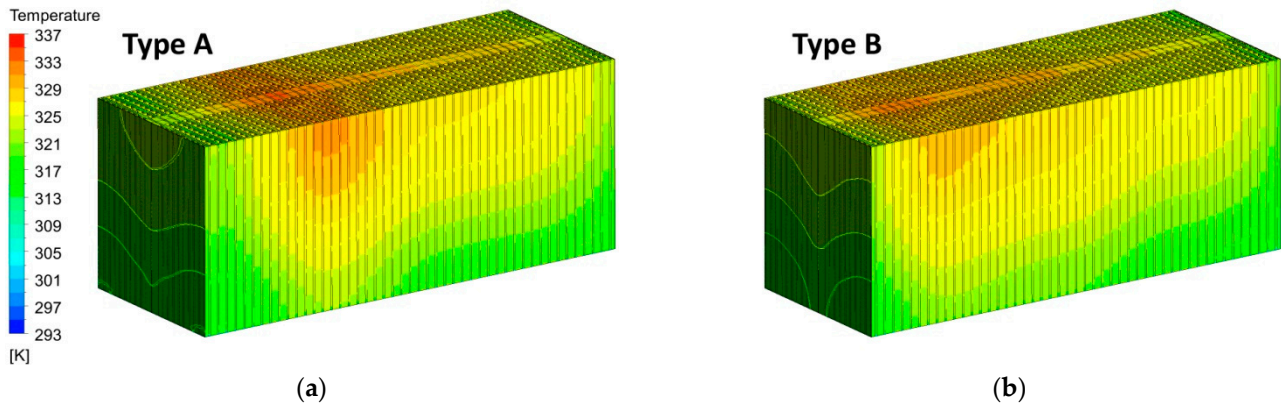


Figure 15. Temperature distribution on the proton-exchange membrane (PEM) stack across (a) Type A and (b) Type B.

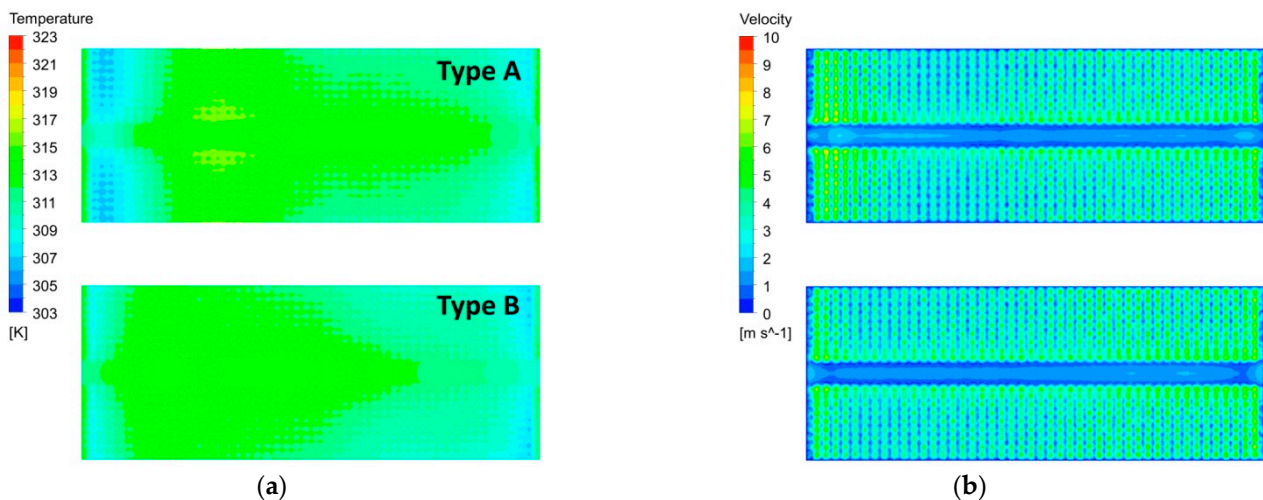


Figure 16. Temperature distribution and velocity profile on section area of PEMFC outlet in (a) Type A and (b) Type B.

The uniformity of the temperature distribution can be assessed using the homogeneity factor (temperature uniformity coefficient). The coefficient can be determined as the ratio of the temperature value to its maximum. Temperature uniformity coefficient represents the balanced distribution of temperature on the outlet surface of the PEMFC as follows:

$$\varepsilon = \frac{T_{AVG}}{T_{MAX}} \cdot 100 \quad (8)$$

Based on the performed simulations, the Type B modification (rounded covers and blades) was chosen for the final adjustment of the PEMFC cooling channel. The rounded covers were made of a plastic tube with a diameter of $D = 25$ mm and were fixed to the sides of the cooling channel by gluing. The straight blades were made of thin steel sheets

and were also glued to the sides of the channel. The blades were adjusted to have a slight inclination with respect to the cooling air inlet from the fan; see Figure 17.

After adjusting the cooling channel, the PEMFC stack was reassembled, and its parameters were measured. To validate the results of the cooling duct optimization, a load of $P = 1000\text{ W}$ was applied, in which the PEMFC showed a local overheating of the plates in the vicinity of the fan inlet.

Figure 18 shows the measurement of the PEMFC temperature using an infrared camera on the surface of the cooling air outlet. Figure 18a shows the original state of PEMFC without performed optimization, and Figure 18b shows the temperature distribution with an optimized cooling channel according to Type B.

Measurement of the PEMFC surface temperature shows that the modification leads to a temperature reduction and a more accurate heat distribution across the stack. The measurements also show that the temperature difference between the original and optimized variant of the cooling duct design is approximately 7 K, which was also shown by the performed CFD simulations; see Figures 13 and 15.

Table 4. Output values from analysis of CFD model.

FC Construction Parts	Original	Type A	Type B
Mass Flow, [kg s^{-1}]	0.0565	0.0565	0.0565
Enthalpy Difference— Δh , [J kg^{-1}]	18,036	18,525	18,644
Unit Heat in Coolant— Q_u , [J s^{-1}]	1020	1045	1053
Outlet Average Temperature— T_{avg} , [K]	312.0	311.8	311.7
Outlet Max Temperature— T_{max} , [K]	325.4	315.8	314.8
Outlet Min Temperature— T_{min} , [K]	301.8	305.9	306.3
Temperature Uniformity, [%]	95.8	98.7	98.9

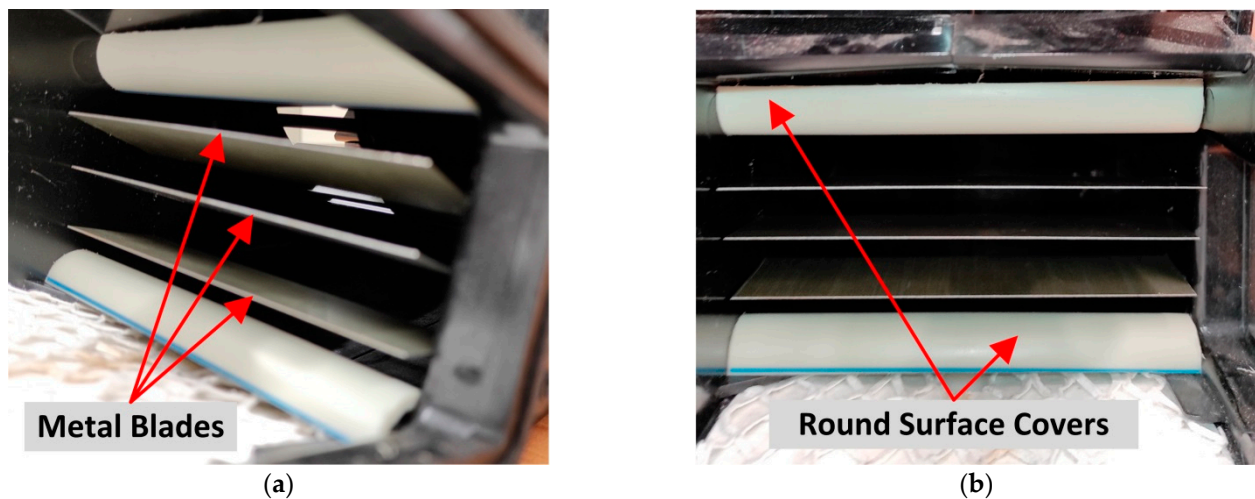


Figure 17. Adjustment of cooling duct close to the fan outlet seen in (a) side view and (b) front view.

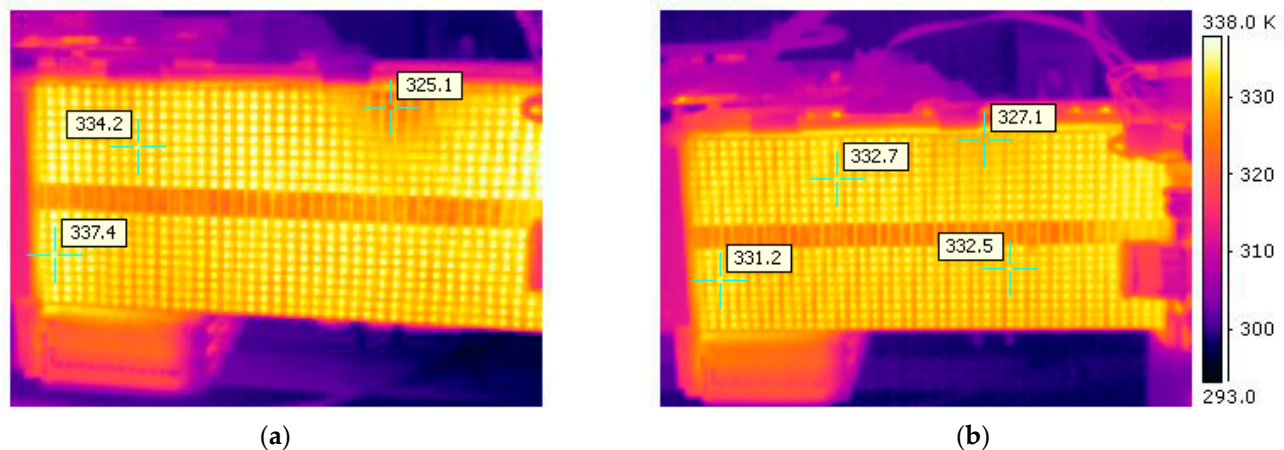


Figure 18. NEXA PEMFC stack IR-thermography at loads $P = 1000$ W in (a) original design and (b) modified cooling duct (Type B).

4. Conclusions

In this work, a concept of the HHS based on low-temperature NEXA Ballard PEMFC is presented. IR measurements and CFD analysis of the FC stack determined problematic overheated zones of the NEXA FC due to unequal heat distribution (air-cooling distribution) across the stack during high loads. Ways of the FC heat transfer optimization were studied. To avoid local overheating of the stack at the air-cooling inlet side, the modification of the original cooling duct was provided. The heat transfer computer simulation of the PEMFC with different cooling duct designs allowed us to determine the optimal conditions for the NEXA stable working and sufficient cooling at high loads around $P_{el} = 1\text{--}1.2$ kW.

In search of a more advantageous shape of the inlet shape of the PEMFC cooling duct, we have performed a number of analyses and simulations of the flow in the cooling duct. We have selected the most interesting results for our publication.

The basic entry condition for these analyses was to preserve the original FC cooling duct design/structure as much as possible. Our solution is therefore a compromise between preserving the original construction and the necessary modification of the inlet shape of the duct, which leads to an improvement in the PEMFC cooling. From this point of view, our solution is also optimal because we have achieved by simple means (glued covers and blades) the improvement of the FC cooling and temperature distribution of the PEMFC stack. The internal protrusions cannot be easily removed due to the stability of the inlet fan mount. The inner protrusions form stabilizing elements that ensure resistance to the deformation of the channel structure. The inlet part of the duct, which is attached to the fan bases of these protrusions, increases the overall stiffness of the plastic structure.

Of course, it is possible to create a new shape of the cooling channel, in which the protrusions in the inlet of the channel will be on its outer part. Such a construction can be realized, for example, by means of 3D printing. However, in the upper part of the duct, this method is impossible for application due to the overlap (dimensions) of the fan. By removing the protrusions in the lower part, the rigidity of the system will be significantly reduced.

Our main goal was the stability of the operation of PEMFC, especially at operating conditions close to the maximum values. Original FC showed instability of operation even before reaching the declared maximum output power ($P = 1200$ W), and the PEMFC was automatically switched off due to an over-temperature state.

The CFD model of the FC was built with significant simplification. The model has been based on the complicated sandwich structure with mutually coupled chemical, electrical, and thermal processes that were assessed rather from a macroscopic point of view of heat dissipation and its effective removal from the FC body.

However, even this applied simplified model shows an unsuitable construction of the cooling channel. Using the CFD model, the influence of several modifications of the inlet part of the duct to achieve higher cooling efficiency was evaluated. On a real PEMFC, this channel modification was performed and a validation measurement of the operating condition and a measurement of the surface temperature of the PEMFC stack were performed. Although the reduction in temperature may not appear significant, the channel treatment performed resulted in more even temperature distribution and generally stabilized the operation of the PEMFC.

The PEMFC is currently operated in our laboratory tends to work with higher currents ($I > 30$ A); thus, we achieve lower efficiency values ($\eta < 40\%$). The main benefit of the performed analysis and modification of the FC cooling channel is therefore the stability of FC operation at its marginal power ($P > 1000$ W). By modifying the cooling duct, we were able to reduce the operating temperature of the PEMFC and minimize local overheating points. Due to more efficient cooling, the permissible ambient temperature can be slightly exceeded while maintaining the stability of PEMFC operation. We have also measured the operation parameters of the FC with an optimized cooling duct. The FC efficiency has occurred in the range shown in Figure 8.

The next possible waste heat utilizing from the stack could be applied for the LT MH H₂ endothermic desorption process. The next steps of the research would correspond to the design of the optimal solution for sufficient heat exchange between NEXA FC and MH storage tank. Most likely, this solution will be based on the direct use of hot exhaust air from the top part of the stack for MH storage heating, without additional heating the liquid heat carrier and using a gas–liquid heat exchanger.

Author Contributions: Conceptualization, A.C. and P.K.; methodology, A.C.; software, P.K.; validation, A.C., P.K., and P.M.; formal analysis, A.C. and P.K.; investigation, A.C., P.K., and P.M.; data curation, P.K.; writing—original draft preparation, A.C.; writing—review and editing, A.C. and P.K.; visualization, P.K. and P.M.; supervision, A.C. All authors have read and agreed to the published version of the manuscript.

Funding: This research was funded by the internal funding program of the VSB—Technical University of Ostrava, identification no: SP2021/20, and by the project TK03020027: Center of Energy and Environmental Technologies.

Data Availability Statement: Not applicable.

Conflicts of Interest: The authors declare no conflict of interest.

Abbreviations

The following abbreviations and symbols are used in this manuscript:

AEM	Anion-Exchange Membrane
CFD	Computational Fluid Dynamics
CL	Catalyst Layers
FC	Fuel Cell
FP	Flow Plates
GDL	Gas Diffusion Layers
HHS	Hydrogen Hybrid Energy System
HT	High-Temperature
IR	Infrared
LHV	Lower-Heating Value
LT	Low-Temperature
MH	Metal Hydride
PEM	Proton-Exchange Membrane
PtG	Power-to-Gas
PV	Photovoltaic
PVC	Polyvinyl Chloride
RES	Renewable Sources

References

1. Hirscher, M. *Handbook of Hydrogen Storage: New Materials for Future Energy Storage*; Wiley-VCH: Weinheim, Germany, 2009; ISBN 9783527322732.
2. Ursúa, A.; San Martín, I.; Barrios, E.L.; Sanchis, P. Stand-alone operation of an alkaline water electrolyser fed by wind and photovoltaic systems. *Int. J. Hydrog. Energy* **2013**, *38*, 14952–14967. [[CrossRef](#)]
3. Barbir, F. PEM electrolysis for production of hydrogen from renewable energy sources. *Sol. Energy* **2005**, *78*, 661–669. [[CrossRef](#)]
4. Yilanci, A.; Dincer, I.; Ozturk, H.K. A review on solar-hydrogen/fuel cell hybrid energy systems for stationary applications. *Prog. Energy Combust. Sci.* **2009**, *35*, 231–244. [[CrossRef](#)]
5. Yunez-Cano, A.; de González-Huerta, R.G.; Tufiño-Velázquez, M.; Barbosa, R.; Escobar, B. Solar-hydrogen hybrid system integrated to a sustainable house in Mexico. *Int. J. Hydrog. Energy* **2016**, *41*, 19539–19545. [[CrossRef](#)]
6. Thomas, C.; James, B.D.; Lomax, F.D.; Kuhn, I.F. Fuel options for the fuel cell vehicle: Hydrogen, methanol or gasoline? *Int. J. Hydrog. Energy* **2000**, *25*, 551–567. [[CrossRef](#)]
7. Hwang, J.; Chang, W.; Weng, F.; Su, A.; Chen, C. Development of a small vehicular PEM fuel cell system. *Int. J. Hydrog. Energy* **2008**, *33*, 3801–3807. [[CrossRef](#)]
8. Mehta, V.; Cooper, J.S. Review and analysis of PEM fuel cell design and manufacturing. *J. Power Sources* **2003**, *114*, 32–53. [[CrossRef](#)]
9. Yamada, Y.; Ueda, A.; Shioyama, H.; Kobayashi, T. High-throughput screening of PEMFC anode catalysts by IR thermography. *Appl. Surf. Sci.* **2004**, *223*, 220–223. [[CrossRef](#)]
10. Moldrik, P.; Chesalkin, A.; Minarik, D. Infrared thermography and computer simulation in research of PEM fuel cells. In Proceedings of the 2019 20th International Scientific Conference on Electric Power Engineering (EPE), Kouty nad Desnou, Czech Republic, 15–17 May 2019. [[CrossRef](#)]
11. Burheim, O.S.; Su, H.; Hauge, H.H.; Pasupathi, S.; Pollet, B.G. Study of thermal conductivity of PEM fuel cell catalyst layers. *Int. J. Hydrog. Energy* **2014**, *39*, 9397–9408. [[CrossRef](#)]
12. Pinar, F.J.; Rastedt, M.; Pilinski, N.; Wagner, P. Characterization of HT-PEM membrane-electrode-assemblies. In *High Temperature Polymer Electrolyte Membrane Fuel Cells*; Springer International Publishing: Cham, Switzerland, 2016; pp. 353–386. ISBN 9783319170817. [[CrossRef](#)]
13. Kopriva, M.; Minarik, D.; Sokansky, K. Setting up and Possibilities of increasing of Operation Voltage of the PEM FC. In Proceedings of the 2007 8th International Scientific Conference Electric Power Engineering (EPE), Kouty nad Desnou, Czech Republic, 6–8 June 2007; pp. 186–198, ISBN 978-80-248-1391-2.
14. Srinivasan, S. *Fuel Cells*; Springer: Boston, MA, USA, 2006; ISBN 9780387251165. [[CrossRef](#)]
15. EG&G Technical Services, Inc. *Seventh Edition Fuel Cell Handbook*; Office of Scientific and Technical Information (OSTI): Pittsburgh, PA, USA, 2004. [[CrossRef](#)]
16. Barbir, F. *PEM Fuel Cells: Theory and Practice*, 2nd ed.; Academic Press: San Diego, CA, USA, 2012; ISBN 9780123877109.
17. Badwal, S.P.S.; Giddey, S.S.; Munnings, C.; Bhatt, A.I.; Hollenkamp, A.F. Emerging electrochemical energy conversion and storage technologies. *Front. Chem.* **2014**, *2*, 79. [[CrossRef](#)]
18. Züttel, A. Materials for hydrogen storage. *Mater. Today* **2003**, *6*, 24–33. [[CrossRef](#)]
19. Godula-Jopek, A. *Hydrogen Production: By Electrolysis*; Wiley-VCH: Weinheim, Germany, 2015; ISBN 9783527333424.
20. Basile, A.; Iulianelli, A. (Eds.) *Advances in Hydrogen Production, Storage and Distribution*; Woodhead Publishing: Cambridge, UK, 2014; ISBN 9780857097682. [[CrossRef](#)]
21. Shcherbakova, L.G.; Dan'ko, D.B.; Muratov, V.B.; Kossko, I.A.; Solonin, Y.M.; Kolbasov, G.Y.; Rusetskii, I.A. Metal hydride use for solar energy accumulation. In *NATO Security through Science Series A: Chemistry and Biology*; Springer: Dordrecht, The Netherlands, 2007; pp. 699–706. ISBN 9781402055126. [[CrossRef](#)]
22. Corgnale, C.; Hardy, B.; Motyka, T.; Zidan, R. Metal hydride based thermal energy storage system requirements for high performance concentrating solar power plants. *Int. J. Hydrog. Energy* **2016**, *41*, 20217–20230. [[CrossRef](#)]
23. Flanagan, T.B.; Oates, W.A. Thermodynamics of intermetallic compound-hydrogen systems. In *Topics in Applied Physics*; Springer: Berlin/Heidelberg, Germany, 1988; pp. 49–85. ISBN 9783540183334. [[CrossRef](#)]
24. Griessen, R.; Riesterer, T. Heat of formation models. In *Topics in Applied Physics*; Springer: Berlin/Heidelberg, Germany, 1988; pp. 219–284. ISBN 9783540183334. [[CrossRef](#)]
25. Fukai, Y.; Okuma, N. Formation of superabundant vacancies in Pd hydride under high hydrogen pressures. *Phys. Rev. Lett.* **1994**, *73*, 1640–1643. [[CrossRef](#)]
26. Chesalkin, A.; Martaus, A.; Averina, J.M.; Men'shikov, V.V. La–Ni based alloy modification by Ce and Fe for the next hydrogen storage in low-temperature metal hydrides. *Russ. J. Non-Ferr. Met.* **2019**, *60*, 492–498. [[CrossRef](#)]
27. Jepsen, J.; Milanese, C.; Puzskiel, J.; Girella, A.; Schiavo, B.; Lozano, G.; Capurso, G.; von Colbe, J.M.B.; Marini, A.; Kabelac, S.; et al. Fundamental material properties of the 2LiBH₄-MgH₂ reactive hydride composite for hydrogen storage: (I) thermodynamic and heat transfer properties. *Energies* **2018**, *11*, 1081. [[CrossRef](#)]
28. Jepsen, J.; Milanese, C.; Puzskiel, J.; Girella, A.; Schiavo, B.; Lozano, G.A.; Capurso, G.; Von Colbe, J.M.B.; Marini, A.; Kabelac, S.; et al. Fundamental Material Properties of the 2LiBH₄-MgH₂ Reactive Hydride Composite for Hydrogen Storage: (II) Kinetic Properties. *Energies* **2018**, *11*, 1170. [[CrossRef](#)]
29. Li, Q.; Liu, Z.; Sun, Y.; Yang, S.; Deng, C. A review on temperature control of proton exchange membrane fuel cells. *Processes* **2021**, *9*, 235. [[CrossRef](#)]

30. Shahsavari, S.; Desouza, A.; Bahrami, M.; Kjeang, E. Thermal analysis of air-cooled PEM fuel cells. *Int. J. Hydrog. Energy* **2012**, *37*, 18261–18271. [[CrossRef](#)]
31. Andisheh Tadbir, M.; Shahsavari, S.; Bahrami, M.; Kjeang, E. Thermal management of an air-cooled PEM fuel cell: Cell level simulation. In Proceedings of the ASME 2012 10th International Conference on Fuel Cell Science, Engineering and Technology; American Society of Mechanical Engineers, San Diego, CA, USA, 23–26 July 2012. [[CrossRef](#)]
32. Al-Baghdadi, M.A.S.; Al-Janabi, H.A.S. Modeling optimizes PEM fuel cell performance using three-dimensional multi-phase computational fluid dynamics model. *Energy Convers. Manag.* **2007**, *48*, 3102–3119. [[CrossRef](#)]
33. An, Q.; Hortig, D.; Merklein, M. Infrared thermography as a new method for quality control of sheet metal parts in the press shop. *Arch. Civ. Mech. Eng.* **2012**, *12*, 148–155. [[CrossRef](#)]
34. Cerdeira, F.; Vázquez, M.; Collazo, J.; Granada, E. Applicability of infrared thermography to the study of the behaviour of stone panels as building envelopes. *Energy Build.* **2011**, *43*, 1845–1851. [[CrossRef](#)]
35. Wang, H.; Li, H.; Yuan, X.-Z. *PEM Fuel Cell Diagnostic Tools: PEM Fuel Cell Diagnostic Tools*; CRC Press: Boca Raton, FL, USA, 2011; Volume 2, ISBN 9781439839195.
36. Das, P.K.; Weber, A.Z.; Bender, G.; Manak, A.; Bittinat, D.; Herring, A.M.; Ulsh, M. Rapid detection of defects in fuel-cell electrodes using infrared reactive-flow-through technique. *J. Power Sources* **2014**, *261*, 401–411. [[CrossRef](#)]
37. Mzoughi, D.; Allagui, H.; Bouaicha, A.; Mami, A. Modeling and testing of a 1.2-kW Nexa fuel cell using bond graph methodology: Modeling and Testing of PEM Fuel Cell Using Bond Graph. *IEEJ Trans. Electr. Electron. Eng.* **2015**, *10*, 527–538. [[CrossRef](#)]
38. Allagui, H.; Mzoughi, D.; Bouaicha, A.; Mami, A. Modeling and simulation of 1.2 kW Nexa PEM fuel cell system. *Indian J. Sci. Technol.* **2016**, *9*. [[CrossRef](#)]
39. Ballard Power Systems Inc. *Nexa Power Module User's Manual, MAN5100078 (310-0027)*; Ballard Power Systems Inc.: Burnaby, BC, Canada, 2003.
40. Franc, J.; Pechanek, R.; Kindl, V.; Zavrel, M. Ventilation system with skewed rotor cooling ducts of 40-MW synchronous machine: A case study. *Electr. Eng.* **2019**, *101*, 203–211. [[CrossRef](#)]
41. Veg, L.; Skalicky, M.; Pechanek, R. Tuning of the thermal model of synchronous machine with PM by real measurement. In Proceedings of the 2020 19th International Conference on Mechatronics—Mechatronika (ME), Prague, Czech Republic, 2–4 December 2020. [[CrossRef](#)]
42. Barbir, F. Fuel Cell Operating Conditions. In *PEM Fuel Cells: Theory and Practice*; Academic Press: Cambridge, MA, USA, 2005; pp. 115–145. ISBN 9780120781423. [[CrossRef](#)]
43. Hasani, M.; Rahbar, N. Application of thermoelectric cooler as a power generator in waste heat recovery from a PEM fuel cell—An experimental study. *Int. J. Hydrog. Energy* **2015**, *40*, 15040–15051. [[CrossRef](#)]